Journal of Materials Chemistry A

A safe and fast-charging lithium-ion battery anode using MXene supported Li3VO4

Journal:	*Journal of Materials Chemistry A*
Manuscript ID	TA-ART-02-2019-002037.R1
Article Type:	Paper
Date Submitted by the Author:	02-Apr-2019
Complete List of Authors:	Huang, Yanghang; Georgia Institute of Technology College of Engineering, School of Chemical & Biomolecular Engineering Yang, Haochen; Georgia Institute of Technology, School of Chemical & Biomolecular Engineering Zhang, Yi; Nanjing Tech University, College of Energy Zhang, Yamin; Georgia Institute of Technology, School of Chemical & Biomolecular Engineering Wu, Yutong; Georgia Institute of Technology Tian, Mengkun; Georgia Institute of Technology, Institute for Electronics and Nanotechnology Chen, Peng; Northeastern University, School of Metallurgy; Georgia Institute of Technology, School of Chemical & Biomolecular Engineering Trout, Robert; Georgia Institute of Technology College of Engineering, School of Chemical & Biomolecular Engineering Ma, Yao; Georgia Institute of Technology, School of Chemical and Biomolecular Engineering Wu, Tzuho; Georgia Institute of Technology College of Engineering, School of Chemical & Biomolecular Engineering Wu, Yuping; Nanjing Tech University, Energy Science and Engineering Liu, Nian; Georgia Institute of Technology, Chemical and Biomolecular Engineering

Journal of Materials Chemistry A

ARTICLE

A safe and fast-charging lithium-ion battery anode using MXene supported Li_3VO_4

Received 00th January 20xx,
Accepted 00th January 20xx

DOI: 10.1039/x0xx00000x

www.rsc.org/

Yanghang Huang,[†a] Haochen Yang,[†a] Yi Zhang,*[ab] Yamin Zhang,[a] Yutong Wu,[a] Mengkun Tian,[c] Peng Chen,[a] Robert Trout,[a] Yao Ma,[a] Tzuho Wu,[a] Yuping Wu*[b] and Nian Liu*[a]

During fast charging, the commonly used Li-ion battery anode material graphite has a significant shortcoming that its discharge potential is too low to guarantee the safety of batteries. Li_3VO_4 (LVO), an alternative anode material, has a safe discharge potential window of 0.5 V to 1.0 V vs. Li^+/Li and high theoretical capacity (~394 mAh/g). However, the poor conductivity of LVO (~10^{-10} S/m) constrains its further applications. In this paper, we innovatively embedded uniform LVO onto a multilayered material, $Ti_3C_2T_x$ MXene, by a sol-gel method. The $Ti_3C_2T_x$ MXene nanolayers with high electrical conductivity (2.4×10^5 S/m) served as the scaffold to load LVO nanoparticles. The LVO/$Ti_3C_2T_x$ MXene composite exhibited remarkable electrochemical performance in terms of rate capability and long-term cycle stability in comparison with bare LVO and commercial graphite anode. LVO/$Ti_3C_2T_x$ MXene composite delivered an initial capacity of ~187 mAh/g and 146 mAh/g after 1000 cycles at 5 C, compared to bare LVO (an initial capacity of ~41 mAh/g and ~40 mAh/g after 1000 cycles at 5 C) and graphite (~71 mAh/g after 1000 cycles at 5 C). This work opens new possibilities of anode materials for safe and fast-charging Li-ion batteries.

Introduction

Lithium-ion batteries (LIBs) have been extensively applied in modern portable electronics, and have a high potential to revolutionize transportation[1–7]. One of the major concerns impeding the acceptance of electric transportation is the long charging time. Fast-charging batteries which are capable of being fully charged within 15 minutes is highly desirable for Electric Vehicle (EV)[8]. However, safety problems arise as batteries are charged at high rates. Also, the size of LIBs used for an electric vehicle is ~10,000 times larger than that in a portable electronic device[4]. As the size of battery grows, the safety issue in LIBs becomes more challenging to manage. The thermal-runaway reaction could occur in each cell, and it can cause a chain reaction that could potentially lead the whole battery to catch fire and even explode[9–11].

The most commonly used anodes: graphite[12], $Li_4Ti_5O_{12}$ (LTO) and silicon have different drawbacks in application in large-scale and fast-charging battery system. Specifically, the discharge potential of graphite[13] is too close to the Li dendrite formation potential, thus Li dendrite is likely to form on the surface of anode during cycling, which potentially leads to the internal short circuit, electrolyte ignition and even catastrophic explosion[14,15]. Worth mentioning, the possibility of dendrite formation is likely to increase with the increment of charging current. Although LTO[13,16] has a higher discharge potential, it suffers from low theoretical specific capacity (175 mAh/g) and excessively high discharge-plateau (~1.5 V vs. Li^+/Li), which limit the overall voltage output and hinder its industrial perspective. Si anode[17–22] can achieve ultra-high theoretical capacity (~4200 mAh/g), nevertheless its substantial volume change due to alloying mechanism at particle-level and electrode-level during cycling is still difficult to manage[3,23]. There still lacks a single anode material specifically designed for fast-charging batteries that simultaneously has safe and moderate operating potential, high theoretical capacity and long cycle life.

Li_3VO_4 (LVO) has recently emerged as a promising anode material of LIBs for its suitable discharge potential window (around 0.5-1.0 V vs. Li^+/Li), high theoretical capacity (394 mAh/g) and long cycle life[24–27], rendering it as a promising anode material for fast-charging LIBs. These advantages make LVO especially suitable for large-scale, fast charging LIBs. However, pure LVO suffers from extremely low

[a] School of Chemical and Biomolecular Engineering, Georgia Institute of Technology, Atlanta, GA 30332, USA
[b] College of Energy and Institute for Electrochemical Energy Storage, Nanjing Tech University, Nanjing 211816, Jiangsu Province, China
[c] Institute for Electronics and Nanotechnology, Georgia Institute of Technology, Atlanta, GA 30332, USA

† These authors contributed equally to this work.
Electronic Supplementary Information (ESI) available: [details of any supplementary information available should be included here]. See DOI: 10.1039/x0xx00000x

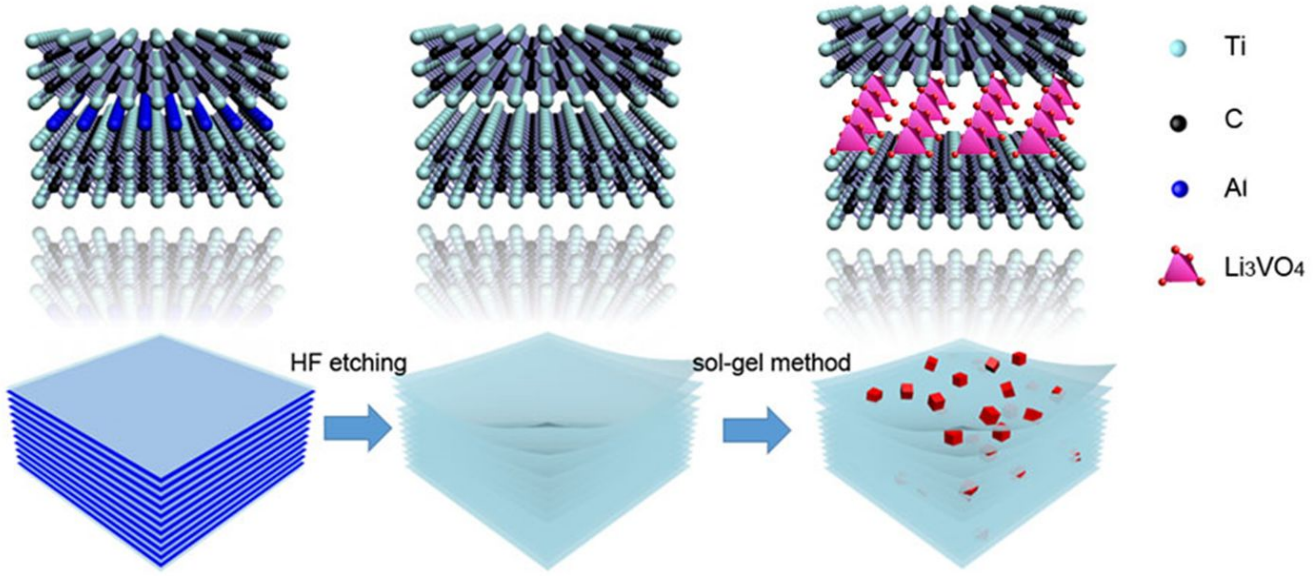

Scheme 1 Schematic illustration of LVO/$Ti_3C_2T_x$ MXene composite preparation

electrical conductivity (~10^{-10} S/m)[28], which significantly reduces the specific capacity. Several approaches have been studied to increase the conductivity of LVO, such as morphology modification, surface coating and ion doping[29–32]. Moreover, the highly conductive carbon materials, such as graphene[33–37] and carbon nanotubes[38] have also been reported as good candidates of anode material hosts[39].

Recently, MXene, a new class of two-dimensional layered transition metal carbides, carbonitrides and nitrides, becomes a promising host of active materials of electrode[21]. MXene has a structure in which closely packed metal atoms are filled with carbon atoms, which makes it metallic conductivity (2.4 × 10^5 S/m)[40–42], ~10^{15} times higher than pure LVO. The precursor of MXene, MAX, is usually ternary carbide or nitride with a general formula $M_{n+1}AX_n$, where M is an early transition metal, A is usually a group 13 or 14 element, and X is either carbon or nitrogen. MXene is obtained by etching the metal element A of MAX and exhibits multilayered morphology. The MXene composite is $M_{n+1}X_nT_x$ where the T represents oxygen, fluorine or hydroxyl functional groups generated from the etching process[43]. The functional groups on the surface of MXene nanolayers act as hooks that hitch and stabilize the active materials of electrode. Compared to conventional sp2-carbon-based conductive support (graphene, carbon nanotubes) which required the introduction of oxygen-containing functional groups decreasing the electronic conductivity, MXene has intrinsic affinity with metal compounds since MXene's surface atomic is Ti which can strongly bind the O atomic of LVO (Fig. S1) and doesn't require any pre-treatment and show a much higher conductivity. The comparison of conductivity between various conductive supports are shown in Table S1. Owing to the outstanding electrical conductivity, layered structure and diversity of chemistry reaction, MXene has been widely applied in many fields, such as detectors, polymer additives, hybridization medium, catalysis and electrochemical energy storage systems[44–49]. Till now, more than sixty different MXene have been discovered, and more possible structures and properties have been predicted[45,50].

In this work, for the first time, LVO was uniformly embedded in between the highly conductive multilayered $Ti_3C_2T_x$ MXene to improve the electrochemical performance. The MXene is a two-dimensional conductive layered material which promotes in-plane 2D electron transfer. Since the LVO directly grows on MXene, they have readily access to electron. Meanwhile, liquid electrolyte can infiltrate in between the stacked layers of LVO/$Ti_3C_2T_x$ MXene, which facilitates the Li^+ transport. The overall three-dimensional electronic and ionic transport pathway were formed, which promoted both electron and ion transport during the lithiation and delithiation processes. Unlike the pure LVO cluster, the layered structure of MXene provided 3-D transport channels for the rapid access for lithium ions, thus the LVO/$Ti_3C_2T_x$ MXene composite exhibited higher specific capacity and significantly enhanced cycling performance compared to bare LVO. To synthesize the composite, since MXene is chemically stable[45], we obtained MXene first and subjected it to LVO growth via a sol-gel process. The highly conductive porous LVO/$Ti_3C_2T_x$ MXene structure had an improved electrochemical performance.

Experimental Section

Synthesis of MXene

1g MAX (Ti_3AlC_2, Carbon-Ukraine, ltd.) powder was added to 25 mL 48% hydrofluoric acid (HF, Sigma Aldrich) and stirred for 96 h at 40 °C. The mixture was collected by centrifugation and washed with deionized water five times. The final product ($Ti_3C_2T_x$ MXene) was dried in a vacuum oven at 80 °C for 12 h.

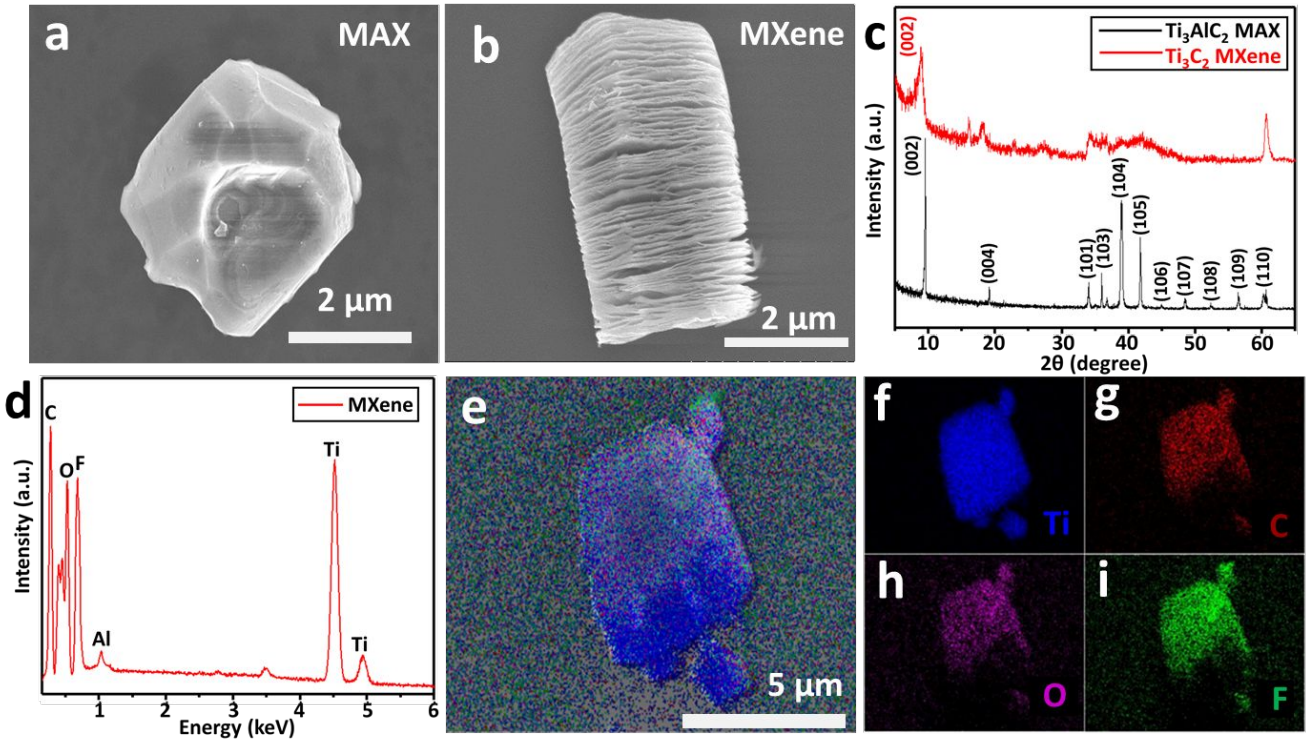

Fig. 1 SEM images of (a) MAX and (b) $Ti_3C_2T_x$ MXene. (c) XRD patterns of MAX (red, top curve) and MXene (black, bottom curve). (d) EDX spectrum and (e-i) EDX mapping of $Ti_3C_2T_x$ MXene.

Synthesis of LVO/$Ti_3C_2T_x$ MXene composite and pure LVO

LVO/$Ti_3C_2T_x$ MXene composite was prepared by sol-gel method. 0.073 g $Ti_3C_2T_x$ MXene powder was added into 100 ml deionized water and the mixture was sonicated for 30 minutes. 1 mmol V_2O_5 (Sigma Aldrich) and 6 mmol $LiOH{\cdot}H_2O$ (Alfa Aesar) were added into the mixture and stirred for 2 h at room temperature. The mixture was dried at 80 °C and then the precursor powders were subsequently treated at 600 °C for 2 h in argon flow to form LVO/ $Ti_3C_2T_x$ MXene composites. According to the mass ratio of $Ti_3C_2T_x$ MXene/V_2O_5 in the precursor mixture, we estimated that the mass ratio of $Ti_3C_2T_x$ MXene and LVO is around 1: 4. MXene is thermally and chemically stable under the synthesis condition[45]. The schematic illustration of LVO/$Ti_3C_2T_x$ MXene preparation is shown in Scheme 1. Pure LVO was also prepared by sol-gel method as described previously with 1 mmol V_2O_5 and 6 mmol $LiOH{\cdot}H_2O$ in 100 ml deionized water.

Material characterization and electrochemical test

The X-ray diffraction (XRD) patterns of nanomaterial were collected using Panalytical XPert PRO Alpha-1. The morphology and crystal structure were examined by scanning electron microscopy (SEM, Hitachi SU8230) and high-resolution transmission electron microscopy (HRTEM, Hitachi HD2700). The tightness test of the LVO/$Ti_3C_2T_x$ MXene composite was operated by ultrasonic bath (Branson 2800).

The working electrodes were made using a slurry method with LVO/$Ti_3C_2T_x$ MXene powders, Carbon Super P (MTI Corporation) and polyvinylidene fluoride (PVDF, MTI Corporation) with a mass ratio of 8:1:1, the mixture was added into N-Methyl-2-pyrrolidone (NMP, Sigma Aldrich) and stirred overnight. The slurry was cast onto copper foil[51] and dried at 80 °C for 12 h. The standard CR2032 type coin cell was assembled in an argon-filled glovebox using the LVO/$Ti_3C_2T_x$ MXene as working electrode and lithium metal foil (Alfa Aesar) as counter electrode. 1M $LiPF_6$ dissolved in ethylene carbonate (EC)/ diethyl carbonate (DEC) (EC/DEC = 1:1 v/v) (Sigma Aldrich) was used as the electrolyte and Celgard 2420 was used as the separator. Cyclic voltammetry (CV) and electrochemical impedance spectroscopy (EIS) measurement were carried out on Bio-Logic VSP potentiostat. The coin cells were tested on an 8-channel battery tester (Wuhan LANHE electronics Corporation) with the voltage window between 0.01 V and 3 V (vs. Li^+/Li). The frequency of EIS measurement ranged from 100 kHz to 0.1 Hz. All the electrochemical measurements were carried out at room temperature. The specific capacity is based on the mass of LVO active material only.

Results and Discussion

Ti_3AlC_2 and MXene

The morphology of MAX and MXene were investigated by SEM. Fig. 1a shows that MAX had smooth edges and dense structure. The particle size of MAX was in the range of 1 to 15 µm (Fig. S2a). The morphology of MXene shows the multilayered structure (Fig. 1b) and relatively rough edges (Fig. S2b). The SEM images clearly indicate that HF treatment led to the removal of Al layers in MAX and exfoliates basal planes.

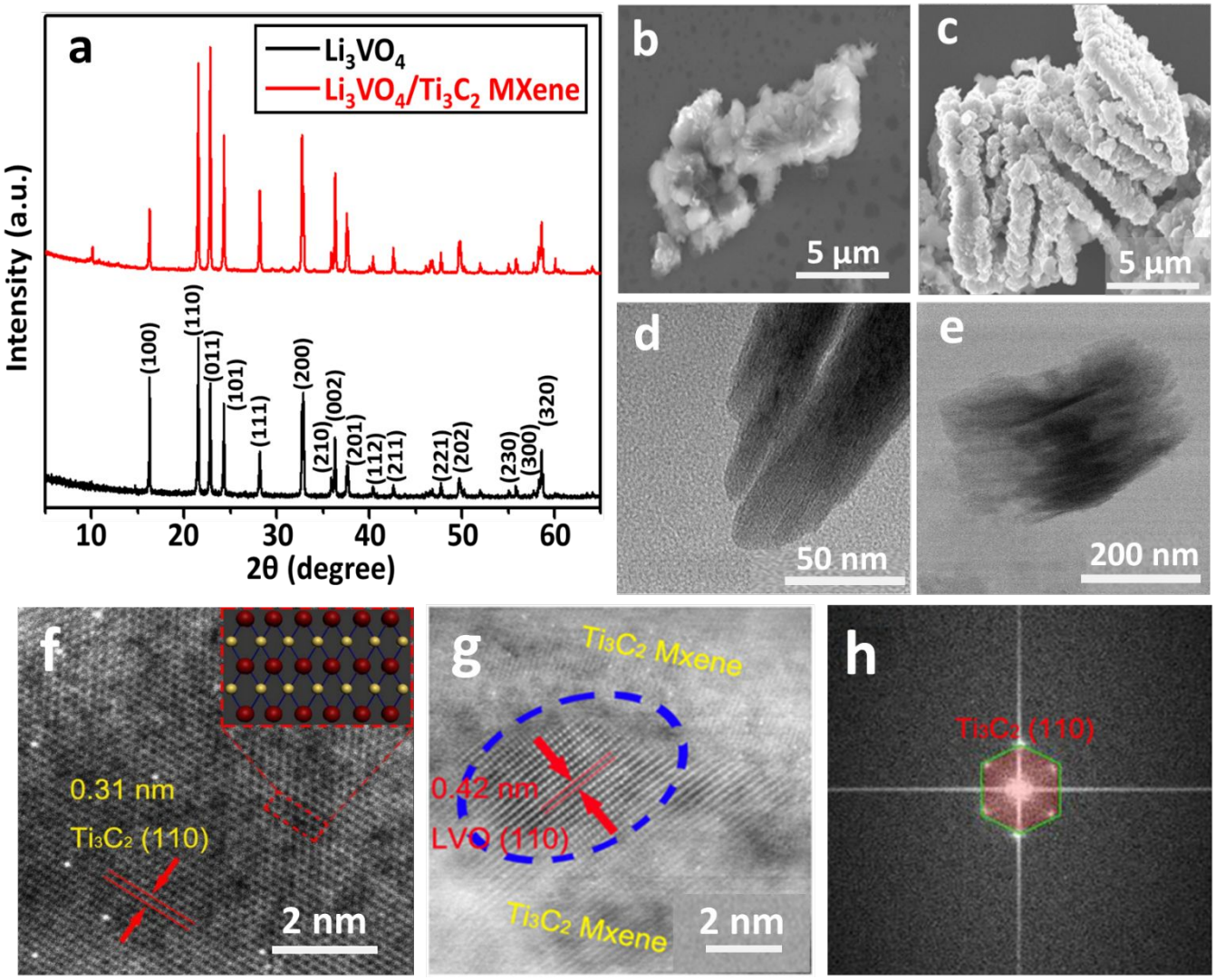

Fig. 2 (a) XRD patterns of LVO (black, bottom curve) and LVO/$Ti_3C_2T_x$ MXene (red, top curve). SEM images of (b) LVO, and (c) LVO/$Ti_3C_2T_x$ MXene. TEM images of (d) $Ti_3C_2T_x$ MXene and (e) LVO/$Ti_3C_2T_x$ MXene. HR-TEM images of (f) $Ti_3C_2T_x$ MXene and (g) LVO/$Ti_3C_2T_x$ MXene. (h) The corresponding FFT pattern of $Ti_3C_2T_x$ MXene.

The crystal structures of MAX and MXene were identified using XRD as shown in Fig. 1c. The diffraction peaks at 2θ = 9.6°, 19.1°, 34.1°, 36.9°, 38.9°, 42.0°, 45.0°, 48.5°, 52.5°, 56.6° and 60.2° belong to the (002), (004), (101), (103), (104), (105), (106), (107), (108), (109) and (110) planes of polycrystalline Ti_3AlC_2 MAX (JCPDS # 52-0875), respectively. After HF treatment, the diffraction peaks at 2θ = 36.9°, 38.9°, 42.0° nearly disappeared, which was attributed to the removal of Al layers. Besides, the characteristic (002) peak at 2θ = 9.6° became broadened and shifted to a lower value (2θ = 8.4°), indicating an increase in c-spacing when the Al atoms were replaced by –F and –OH functional groups. These results are in a good agreement with the previous works[43,52], confirming the successful synthesis of $Ti_3C_2T_x$ MXene.

Energy dispersive X-ray (EDX) was conducted to investigate the elemental distribution of $Ti_3C_2T_x$ MXene in Fig. 1d-i. Based on the EDX spectrum in Fig. 1d, $Ti_3C_2T_x$ MXene was characterized to be composed of Ti, C, O, F and a trace amount of Al which was mostly etched by HF. In contrast, the Al uniformly distributed in the MAX shown by EDX mapping in Fig. S3b. The composition of $Ti_3C_2T_x$ MXene estimated from EDX analysis exhibited the mole ratio of Ti: F: O: Al: C = 1.89: 1.29: 0.7: 0.13: 1, which was close to the stoichiometry of Ti_3C_2. The remaining trace amount of Al in MXene was likely from the reaction product of AlF_3, which could not be fully washed away after reaction. The presence of F and O was ascribed to the surface terminations (–F and –OH), which would enhance the binding between MXene layers and LVO particles in the next step. EDX mapping images (Fig. 1e-i) indicate that the elements of Ti, C, O and F distributed uniformly in $Ti_3C_2T_x$ MXene.

LVO and LVO/MXene

Fig. 2a shows the XRD patterns of the synthesized LVO and LVO/$Ti_3C_2T_x$ MXene. The diffraction peaks with high intensity suggested the good crystallinity of pure LVO. The peaks at approximate 2θ values of 16.0°, 21.5°, 22.6°, 24.2°, 28.1°, 32.8°,

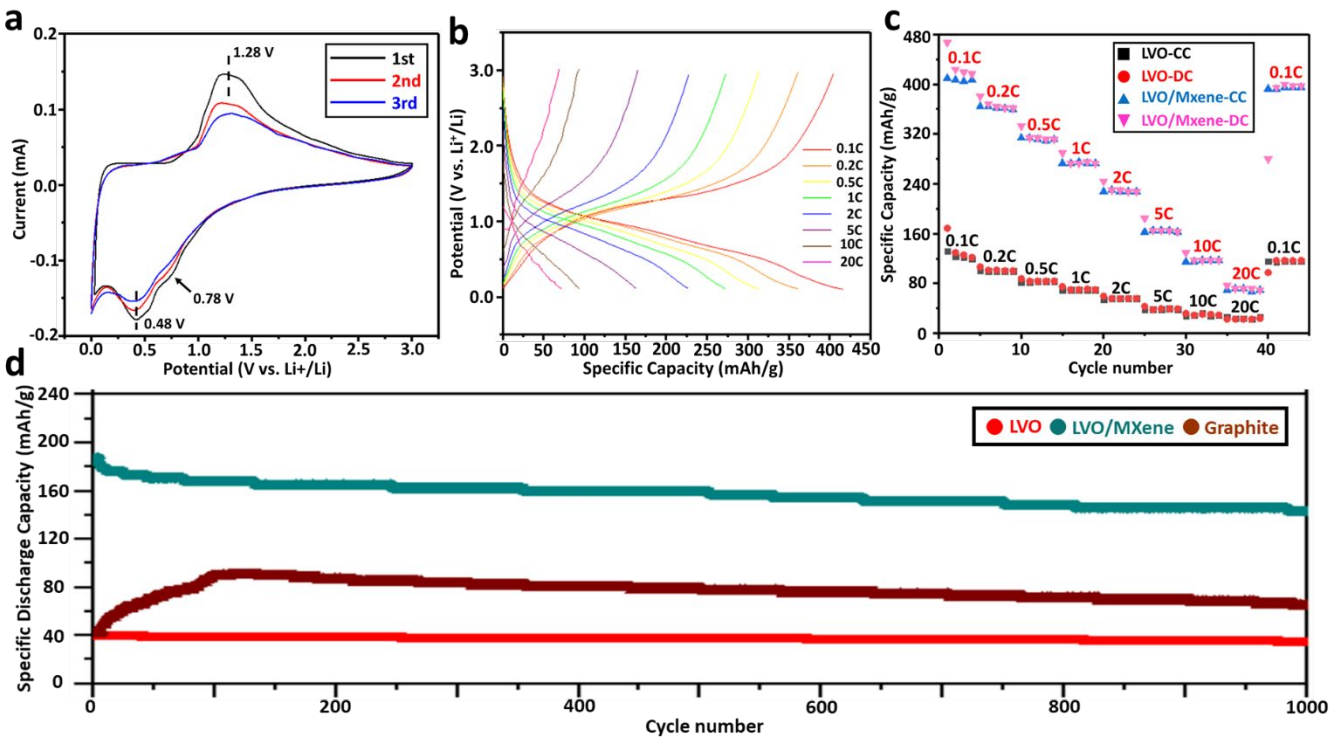

Fig. 3 (a) Cyclic voltammetry (CV) of LVO/$Ti_3C_2T_x$ MXene composite electrode at the scan rate of at 0.2 mV/s, (b) Galvanostatic charge/discharge curves of LVO/Ti_3C_2Tx MXene composite at various C-rates in the voltage window of 0.1 V to 3.0 V. (c) Rate performance of LVO/$Ti_3C_2T_x$ MXene (CC: charge capacity, DC: discharge capacity). (d) Capacity retention under 5 C.

36.1°, 36.5°, 37.6°, 40.5°, 43.2°, 47.8°, 50.5°, 56.6°, 57.4°, 58.5° were attributed to (100), (110), (011), (101), (111), (200), (210), (002), (201), (112), (211), (221), (202), (230), (300) and (320) planes of LVO. The intensity of MXene diffraction peaks in LVO/$Ti_3C_2T_x$ MXene was weak, and only two strongest distinctive peaks of $Ti_3C_2T_x$ MXene were observed, namely (002) plane at 2θ = 8.4° and (110) plane at 2θ = 60.2°, indicating that MXene was only a small fraction of the composite.

The morphology of LVO and LVO/$Ti_3C_2T_x$ MXene composite were characterized by SEM. The pure LVO presented aggregated particles morphology (Fig. 2b). Fig. 2c shows the morphology of LVO/$Ti_3C_2T_x$ MXene composite. The uniform LVO nanoparticles were uniformly grown onto MXene nanosheets. This conclusion is also supported by the EDX of LVO//$Ti_3C_2T_x$ MXene composite in which the elemental mapping for V demonstrates the uniform LVO homogeneously is grown onto MXene nanosheets (Fig. S4), suggesting the successful fabrication of LVO/$Ti_3C_2T_x$ MXene composite.

Compared with previous works (Fig. S5), our LVO/$Ti_3C_2T_x$ MXene composite shows high and uniform coverage of LVO on MXene, as well as between the MXene sheets. The intimate contact between LVO and MXene resulted in facilitating electron transfer which enable the high-C-rate electrochemical performance of LVO/$Ti_3C_2T_x$ MXene composite and remarkable rate capabilities. To test the tightness between LVO particles and MXene layer, the composite was sonicated in deionized water for ten minutes. The morphology of the composite after sonication was characterized by SEM. Although the MXene interlayer space was increased after sonicating, the LVO particles still bound tightly to MXene layers (Fig. S6a and S6b).

The TEM and HRTEM images of $Ti_3C_2T_x$ MXene and LVO/$Ti_3C_2T_x$ MXene samples are shown in Fig. 2d-g. Two-dimensional layered structure of MXene was observed on the edges of the sample (Fig. 2d, S7a). HRTEM image (Fig. 2f) of $Ti_3C_2T_x$ clearly shows the layered structure and the lattice fringe distance as 0.31 nm, which is consistent with the (110) crystal plane of $Ti_3C_2T_x$[53]. The Fast Fourier Transform (FFT) pattern exhibits a symmetrical hexagonal shape (Fig. 2h), indicating the typical hexagonal crystalline structure of $Ti_3C_2T_x$ phase. After LVO incorporation, a large number of LVO nanoparticles formed and uniformly distributed on the surface of $Ti_3C_2T_x$ MXene nanolayers (Fig. S7b). As shown in Fig. 2e, the shadow in the middle of MXene nanolayers indicates the presence of LVO nanoparticles. A lattice spacing of 0.42 nm was observed in HRTEM image of LVO/$Ti_3C_2T_x$ MXene composite (Fig. 2g), an indication of the (110) plane of LVO[24,54].

Electrochemical performance of LVO/$Ti_3C_2T_x$ MXene composite

The cyclic voltammetry (CV) results of LVO/$Ti_3C_2T_x$ MXene composite electrode in the voltage range of 0.1 V to 3 V (vs. Li^+/Li) at the scan rate of 0.2 mV/s are shown in Fig. 3a. In the first cycle, one oxidative peak was noticeable at 1.28 V, while two reductive peaks were found at 0.48 and 0.78 V. The broad and shoulder-like cathodic peak at 0.78 V which was attributed to the formation of solid electrolyte interphase (SEI), disappeared in subsequent cycles. The reductive peak at 0.48 V was assigned to the insertion of Li^+ into

LVO/$Ti_3C_2T_x$ MXene, and the oxidative peak at 1.28 V corresponded to the de-insertion of Li^+ from LVO/$Ti_3C_2T_x$ MXene. The rate capability of LVO/$Ti_3C_2T_x$ MXene electrode was evaluated at various current rates in the voltage window of 0.1 V to 3 V, ranging from 0.1 C to 20 C, as shown in Fig. 3b and 3c. The first cycle charge/discharge curves of LVO/$Ti_3C_2T_x$ MXene composite anode are also shown in Fig. S8. The LVO/$Ti_3C_2T_x$ MXene composite displayed a lithiation voltage plateau around 0.5 V and delithiation voltage plateau around 1.3 V (Fig. 3b), which was consistent with the results of CV test. Fig. 3c shows the reversible capacities of the LVO/$Ti_3C_2T_x$ MXene composite at slow charging (0.1 C, 0.2 C, 0.5 C), fast charging (1 C, 2 C, 5 C), and extremely fast charging (10 C, 20 C) were 420, 362, 311, 272, 230, 165, 117, 71 mAh/g, respectively[8]. The rate performance of the bare MXene is shown in Fig. S9, indicating the capacity contribution of the bare MXene in the overall capacity. After the rate returned to 0.1 C, the capacity of the LVO/$Ti_3C_2T_x$ MXene electrode was recovered to 400 mAh/g, indicating a good cyclability. The discharge specific capacity at 0.1 C is a little bit higher than the theoretical capacity of LVO (394 mAh/g). One possible reason is that our calculation of the capacity is based on the mass of LVO. Moreover, the excess discharge capacity may be attributed to the capacity contribution from $Ti_3C_2T_x$ MXene and the capacitive behaviour of nanosized electrode materials[25]. Furthermore, the LVO/$Ti_3C_2T_x$ MXene composite exhibits good retention of specific capacity in Fig. 3d. Since fast charging is defined as fully charge the EV batteries within 15 minutes[8], the cells were tested at 5 C (2.0 A/g). The initial discharge capacity of LVO/$Ti_3C_2T_x$ MXene composite was 187 mAh/g, which slightly decreased to 146 mAh/g (78% capacity retention) after 1000 cycles. Compared with pure LVO (~40 mAh/g after 1000 cycles at 5 C) and graphite (~71 mAh/g after 1000 cycles at 5 C), the LVO/$Ti_3C_2T_x$ MXene composite shows improved specific capacity. Besides, the coulombic efficiency of LVO/$Ti_3C_2T_x$ MXene composite anode is shown in Fig. S10. Furthermore, LVO/$Ti_3C_2T_x$ MXene composite delivered an initial capacity of ~114 mAh/g and 81 mAh/g after 1000 cycles at extremely fast charging (10 C) as shown in Fig. S11. The rate capability and long-term cycle stability of the LVO/$Ti_3C_2T_x$ MXene anode are compared with other similar LIB anodes, which are summarized in Table S2, showing an improved performance. The good long-cycle stability and improved rate capability were attributed to the unique layered structure and improved conductivity of LVO/$Ti_3C_2T_x$ MXene composite and intimate contact between LVO and $Ti_3C_2T_x$ MXene. Moreover, the $Ti_3C_2T_x$ MXene also buffers the volume change of LVO and maintains the structure of electrode integrity. Fig. S12 shows the SEM images of electrodes before (a) and after (b) 1000 cycles, which demonstrate that the LVO/$Ti_3C_2T_x$ MXene electrode is a hard film and is able to strongly adhere to the current collector after 1000 cycles. In addition, the phase of LVO is demonstrated to be stable in previous works in which the XRD results of the LVO anode before and after cycles suggest that the lithium intercalation reaction in LVO is reversible and the phase structure of LVO is stable after cycling[55–57].

The EIS of the electrodes after three cycles are shown in Fig. S13. Inset of the figure shows the equivalent circuit model for the impedance spectra. R_s is the combination of electrolyte resistance and ohmic resistances of cell components. R_f and R_{ct} are the resistance of SEI film and charge transfer resistance, respectively. According to the simulation results, the R_{ct} of bare LVO anode (184.8 Ω) is much higher than that of LVO/MXene composite anode (74.6 Ω), suggesting a significant charge transfer impedance reduction for the LVO/MXene composite anode. Besides, constant phase element (CPE) represents the double layer capacitance, and the Warburg impedance (Z_W) corresponds to the line at low frequency, which is related to the Li^+ diffusion within the particles[24,34].

The three-dimensional electrical conducting network of highly conductive LVO/$Ti_3C_2T_x$ MXene composite promoted electron transfer during the lithiation and delithiation processes. At the same time, the layered structure of LVO/$Ti_3C_2T_x$ MXene assisted lithiation/delithiation process due to the facilitated Li^+ transport. Overall, the electronic and ionic transport occurred at a faster pace resulting in higher capacity.

Conclusion

In conclusion, our work pioneers a facile approach to uniformly grow battery electrode materials onto MXene. The LVO/$Ti_3C_2T_x$ MXene composite was characterized as a multilayered structure which was composed of highly conductive MXene and LVO with intimate contact, delivering an outstanding capacity of 187 mAh/g at 5 C for the first cycle with a high capacity retention (146 mAh/g after 1000 cycles). In contrast, the pure LVO only delivered 40 mAh/g and the graphite delivered 71 mAh/g at 5 C. The high-power capability of LVO/$Ti_3C_2T_x$ MXene composite was ascribed to the intimate incorporation of nanostructured LVO onto MXene nanolayers, which significantly enhanced the transport kinetics by reducing the electronic and ionic transport pathway. Our work and demonstrates a new chemistry to effectively and uniformly composite MXene with metal compounds and provides a guidance to the design of alternative LIB anode materials used in fast-charging batteries without safety concern.

Conflicts of interest

There are no conflicts to declare.

Acknowledgements

The work was financially supported by faculty startup fund from Georgia Institute of Technology. Material characterization was performed in part at the Georgia Tech Institute for Electronics and Nanotechnology, a member of the National Nanotechnology Coordinated Infrastructure, which is supported by the National Science Foundation (Grant ECCS-1542174). Y.Z. ackowledges support from National Nature Science Foundation of China (51702157), China Postdoctoral Science Foundation (2017M611795), Natural Science Foundation of colleges and universities of Jiangsu Province in China (17KJB150022). Y.W. ackowledges support from National Key R & D Program of China (2018YFB0104301), the Distinguished Young Scientists Program of the National Natural Science Foundation of China (51425301), and NSFC (21374021 and U1601214).

Notes and references

1 S. Chu, Y. Cui and N. Liu, *Nat. Mater.*, 2017, **16**, 16–22.
2 S. Chu and A. Majumdar, *Nature*, 2012, **488**, 294–303.
3 Y. Sun, N. Liu and Y. Cui, *Nat. Energy*, 2016, **1**, 1–12.
4 M. Armand and J. M. Tarascon, *Nature*, 2008, **451**, 652–657.
5 B. Dunn, H. Kamath and J. M. Tarascon, *Science (80-.).*, 2011, **334**, 928–935.
6 Y. Zhang, Y. Jiang, Y. Li, B. Li, Z. Li and C. Niu, *J. Power Sources*, 2015, **281**, 425–431.
7 Y. Wu and N. Liu, *Chem*, 2018, **4**, 438–465.
8 Department of Energy, https://www.energy.gov/eere/vehicles/downloads/enabling-extreme-fast-charging-technology-gap-assessment , (accessed December 2018)
9 Y. Zhang, Y. Wu, H. Ding, Y. Yan, Z. Zhou, Y. Ding and N. Liu, *Nano Energy*, 2018, **53**, 666–674.
10 P. Chen, Y. Wu, Y. Zhang, T.-H. Wu, Y. Ma, C. Pelkowski, H. Yang, Y. Zhang, X. Hu and N. Liu, *J. Mater. Chem. A*, 2018, **6**, 21933–21940.
11 Y. Wu, Y. Zhang, Y. Ma, J. D. Howe, H. Yang, P. Chen, S. Aluri and N. Liu, *Adv. Energy Mater.*, 2018, **8**, 1802470.
12 X. Sun, H. Zhang, L. Zhou, X. Huang and C. Yu, *Small*, 2016, 3732–3737.
13 J. Lu, Z. Chen, F. Pan, L. A. Curtiss and K. Amine, *Nat. Nanotechnol.*, 2016, **11**, 1031–1038.
14 X. Fan, L. Chen, O. Borodin, X. Ji, J. Chen, S. Hou, T. Deng, J. Zheng, C. Yang, S. C. Liou, K. Amine, K. Xu and C. Wang, *Nat. Nanotechnol.*, 2018, **13**, 1–8.
15 Q. Shi, Y. Zhong, M. Wu, H. Wang and H. Wang, *Proc. Natl. Acad. Sci.*, 2018, **115**, 5676–5680.
16 Z. Chen, I. Belharouak, Y. K. Sun and K. Amine, *Adv. Funct. Mater.*, 2013, **23**, 959–969.
17 N. Liu, H. Wu, M. T. McDowell, Y. Yao, C. Wang and Y. Cui, *Nano Lett.*, 2012, **12**, 3315–3321.
18 Y. Zhang and N. Liu, *Chem. Mater.*, 2017, **29**, 9589–9604.
19 N. Liu, Z. Lu, J. Zhao, M. T. Mcdowell, H. W. Lee, W. Zhao and Y. Cui, *Nat. Nanotechnol.*, 2014, **9**, 187–192.
20 Y. Yao, M. T. McDowell, I. Ryu, H. Wu, N. Liu, L. Hu, W. D. Nix and Y. Cui, *Nano Lett.*, 2011, **11**, 2949–2954.
21 Y. Xia, T. S. Mathis, M. Q. Zhao, B. Anasori, A. Dang, Z. Zhou, H. Cho, Y. Gogotsi and S. Yang, *Nature*, 2018, **557**, 409–412.
22 H. Su, A. A. Barragan, L. Geng, D. Long, L. Ling, K. N. Bozhilov, L. Mangolini and J. Guo, *Angew. Chemie - Int. Ed.*, 2017, **56**, 10780–10785.
23 X. H. Liu, L. Zhong, S. Huang, S. X. Mao, T. Zhu and J. Y. Huang, *ACS Nano*, 2012, **6**, 1522–1531.
24 C. Zhang, H. Song, C. Liu, Y. Liu, C. Zhang, X. Nan and G. Cao, *Adv. Funct. Mater.*, 2015, **25**, 3497–3504.
25 Q. Li, Q. Wei, J. Sheng, M. Yan, L. Zhou, W. Luo, R. Sun and L. Mai, *Adv. Sci.*, 2015, **2**, 1–8.
26 Y. Shi, J. Z. Wang, S. L. Chou, D. Wexler, H. J. Li, K. Ozawa, H. K. Liu and Y. P. Wu, *Nano Lett.*, 2013, **13**, 4715–4720.
27 C. Liao, Q. Zhang, T. Zhai, H. Li and H. Zhou, *Energy Storage Mater.*, 2017, **7**, 17–31.
28 L. Shen, H. Lv, S. Chen, P. Kopold, P. A. van Aken, X. Wu, J. Maier and Y. Yu, *Adv. Mater.*, 2017, **29**, 1700142.
29 Z. Liu, H. Li, M. Zhu, Y. Huang, Z. Tang, Z. Pei, Z. Wang, Z. Shi, J. Liu, Y. Huang and C. Zhi, *Nano Energy*, 2018, **44**, 164–173.
30 J. Guo, Q. Liu, C. Wang and M. R. Zachariah, *Adv. Funct. Mater.*, 2012, **22**, 803–811.
31 L. Wang, S. Yue, Q. Zhang, Y. Zhang, Y. R. Li, C. S. Lewis, K. J. Takeuchi, A. C. Marschilok, E. S. Takeuchi and S. S. Wong, *ACS Energy Lett.*, 2017, **2**, 1465–1478.
32 C. Zhang, K. Wang, C. Liu, X. Nan, H. Fu, W. Ma, Z. Li and G. Cao, *NPG Asia Mater.*, 2016, **8**, e287–e287.
33 Z. Jian, M. Zheng, Y. Liang, X. Zhang, S. Gheytani, Y. Lan, Y. Shi and Y. Yao, *Chem. Commun.*, 2015, **51**, 229–231.
34 J. Liu, P. J. Lu, S. Liang, J. Liu, W. Wang, M. Lei, S. Tang and Q. Yang, *Nano Energy*, 2015, **12**, 709–724.
35 Y. Shi, J.-Z. Wang, S.-L. Chou, D. Wexler, H.-J. Li, K. Ozawa, H.-K. Liu and Y.-P. Wu, *Nano Lett.*, 2013, **13**, 4715–4720.
36 H. Zhang, L. Zhou and C. Yu, *RSC Adv.*, 2014, **4**, 495–499.
37 J. Tang, W. Liu, H. Wang and A. Gomez, *Adv. Mater.*, 2016, **28**, 10298–10303.
38 E. Iwama, N. Kawabata, N. Nishio, K. Kisu, J. Miyamoto, W. Naoi, P. Rozier, P. Simon and K. Naoi, *ACS Nano*, 2016, **10**, 5398–5404.
39 H. Liu, P. Hu, Q. Yu, Z. Liu, T. Zhu, W. Luo, L. Zhou and L. Mai, *ACS Appl. Mater. Interfaces*, 2018, **10**, 23938–23944.
40 F. Feng, J. Wu, C. Wu and Y. Xie, *Small*, 2015, **11**, 654–666.
41 M. Ghidiu, M. R. Lukatskaya, M. Q. Zhao, Y. Gogotsi and M. W. Barsoum, *Nature*, 2015, **516**, 78–81.
42 Z. Ling, C. E. Ren, M.-Q. Zhao, J. Yang, J. M. Giammarco, J. Qiu, M. W. Barsoum and Y. Gogotsi, *Proc. Natl. Acad. Sci.*, 2014, **111**, 16676–16681.
43 M. Naguib, M. Kurtoglu, V. Presser, J. Lu, J. Niu, M. Heon, L. Hultman, Y. Gogotsi and M. W. Barsoum, *Adv. Mater.*, 2011, **23**, 4248–4253.
44 M. R. Lukatskaya, O. Mashtalir, C. E. Ren, Y. Dall'Agnese, P. Rozier, P. L. Taberna, M. Naguib, P. Simon, M. W. Barsoum and Y. Gogotsi, *Science*, 2013, **341**, 1502–5.
45 B. Anasori, M. R. Lukatskaya and Y. Gogotsi, *Nat. Rev. Mater.*, 2017, **2**, 16098.
46 X. Wang, S. Kajiyama, H. Iinuma, E. Hosono, S. Oro, I. Moriguchi, M. Okubo and A. Yamada, *Nat. Commun.*, 2015, **6**, 1–6.
47 M. Yu, S. Zhou, Z. Wang, J. Zhao and J. Qiu, *Nano Energy*, 2018, **44**, 181–190.
48 A. VahidMohammadi, J. Moncada, H. Chen, E. Kayali, J. Orangi, C. A. Carrero and M. Beidaghi, *J. Mater. Chem. A*, 2018, **6**, 22123–22133.
49 A. VahidMohammadi, A. Hadjikhani, S. Shahbazmohamadi and M. Beidaghi, *ACS Nano*, 2017, **11**, 11135–11144.
50 M. Khazaei, M. Arai, T. Sasaki, C.-Y. Chung, N. S. Venkataramanan, M. Estili, Y. Sakka and Y. Kawazoe, *Adv. Funct. Mater.*, 2013, **23**, 2185–2192.
51 M. Wang, M. Tang, S. Chen, H. Ci, K. Wang, L. Shi, L. Lin, H. Ren, J. Shan, P. Gao, Z. Liu and H. Peng, *Adv. Mater.*, 2017, **29**, 1–7.
52 M. Alhabeb, K. Maleski, T. S. Mathis, A. Sarycheva, C. B. Hatter, S. Uzun, A. Levitt and Y. Gogotsi, *Angew. Chemie - Int. Ed.*, 2018, **57**, 5444–5448.
53 Y. Zhang, B. Guo, L. Hu, Q. Xu, Y. Li, D. Liu and M. Xu,

J. Alloys Compd., 2018, **732**, 448–453.

54 Y. Yang, J. Li, X. He, J. Wang, D. Sun and J. Zhao, *J. Mater. Chem. A*, 2016, **4**, 7165–7168.

55 S. Liang, W. Wang, S. Tang, P.-J. Lu, J. Liu, M. Lei and Q. Yang, *Nano Energy*, 2015, **12**, 709–724.

56 Z. Liang, Z. Lin, Y. Zhao, Y. Dong, Q. Kuang, X. Lin, X. Liu and D. Yan, *J. Power Sources*, 2015, **274**, 345–354.

57 L. Zhang, J. Ma, X. Yang, S. Ni and X. Lv, *Electrochim. Acta*, 2014, **130**, 800–804.

Graphical Abstract